

SCIENTIFIC REPORTS

OPEN

The 7×1 Fermi Surface Reconstruction in a Two-dimensional f -electron Charge Density Wave System: PrTe_3

Received: 11 February 2016

Accepted: 04 July 2016

Published: 25 July 2016

Eunsook Lee¹, D. H. Kim¹, Hyun Woo Kim¹, J. D. Denlinger², Heejung Kim³, Junwon Kim³, Kyoo Kim^{3,4}, B. I. Min³, B. H. Min^{5,†}, Y. S. Kwon⁵ & J.-S. Kang¹

The electronic structure of a charge density wave (CDW) system PrTe_3 and its modulated structure in the CDW phase have been investigated by employing ARPES, XAS, Pr 4*f*RPES, and first-principles band structure calculation. Pr ions are found to be nearly trivalent, supporting the CDW instability in the metallic Te sheets through partial filling. Finite Pr 4*f* spectral weight is observed near the Fermi level, suggesting the non-negligible Pr 4*f* contribution to the CDW formation through the Pr 4*f*-Te 5*p* hybridization. The two-fold symmetric features in the measured Fermi surface (FS) of PrTe_3 are explained by the calculated FS for the assumed 7×1 CDW supercell formation in Te sheets. The shadow bands and the corresponding very weak FSs are observed, which originate from both the band folding due to the 3D interaction of Te sheets with neighboring Pr-Te layers and that due to the CDW-induced FS reconstruction. The straight vertical FSs are observed along k_z , demonstrating the nearly 2D character for the near- E_F states. The observed linear dichroism reveals the in-plane orbital character of the near- E_F Te 5*p* states.

The charge density wave (CDW) transition is one of the most interesting phase transitions, which occurs due to the Fermi surface (FS) instability^{1,2}, like the Peierls transition in one dimension (1D)³. The CDW formation is often observed in the low-dimensional systems, and so the CDW phenomenon involves the complicated physics realized in the low-dimensional systems⁴. The CDW state also competes with the exotic ground states, such as magnetic ordering and superconductivity^{5,6}. It has been controversial whether the FS nesting is the major driving mechanism for the CDW transitions in the two-dimensional (2D) or three-dimensional (3D) systems or whether there exist some other important mechanisms, such as the peak of the real part of the charge susceptibility, \vec{k} -dependent electron-phonon coupling, and electron-electron interactions^{7–10}. In order to understand the nature of the CDW transition, it is crucial to investigate the electronic structure, including the FS of the system. Recent technical progress in angle-resolved photoemission spectroscopy (ARPES) has made it possible to observe the FS topology and the band structures of the solids with the high resolution. Hence, ARPES has become a very good experimental tool for studying the electronic structures of the CDW systems⁹.

The most extensively studied CDW systems by using ARPES are the quasi-2D transition-metal (*M*) chalcogenides (1*T*-*MX*₂ or 2*H*-*MX*₂; *X* = S, Se, Te)^{6,7,9–11}, and *R*Te₃ (*R*: rare-earth ion)^{4,12–23}. Note, however, that *MX*₂ and *R*Te₃ are quite different in that the electrons responsible for the CDW transition are *M* 3*d* electrons in *MX*₂, whereas those are Te 5*p* electrons in *R*Te₃. Since the on-site Coulomb interaction (*U*) of Te 5*p* electrons is much weaker than that of *M* 3*d* electrons, the electronic structures of *R*Te₃ would be simpler than those of *MX*₂, providing the advantage of studying *R*Te₃ in investigating the CDW mechanism.

As shown in Fig. 1(a), *R*Te₃ crystallizes in the quasi-2D layered orthorhombic (close to tetragonal) structure, having three types of Te sites: Te(1), Te(2), and Te(3). Te(2) and Te(3) atoms form the two planar square sheets,

¹Department of Physics, The Catholic University of Korea, Bucheon 14662, Korea. ²Advanced Light Source (ALS), Lawrence Berkeley Laboratory, Berkeley, CA 12345, USA. ³Department of Physics, Pohang University of Science and Technology, Pohang, 37673, Korea. ⁴MPPC CPM, Pohang University of Science and Technology, Pohang 37673, Korea. ⁵Department of Emerging Materials Science, DGIST, Daegu 42988, Korea. [†]Present address: CeNSCMR, Department of Physics and Astronomy, Seoul National University, Seoul 08826, Korea. Correspondence and requests for materials should be addressed to J.-S.K. (email: kangjs@catholic.ac.kr)

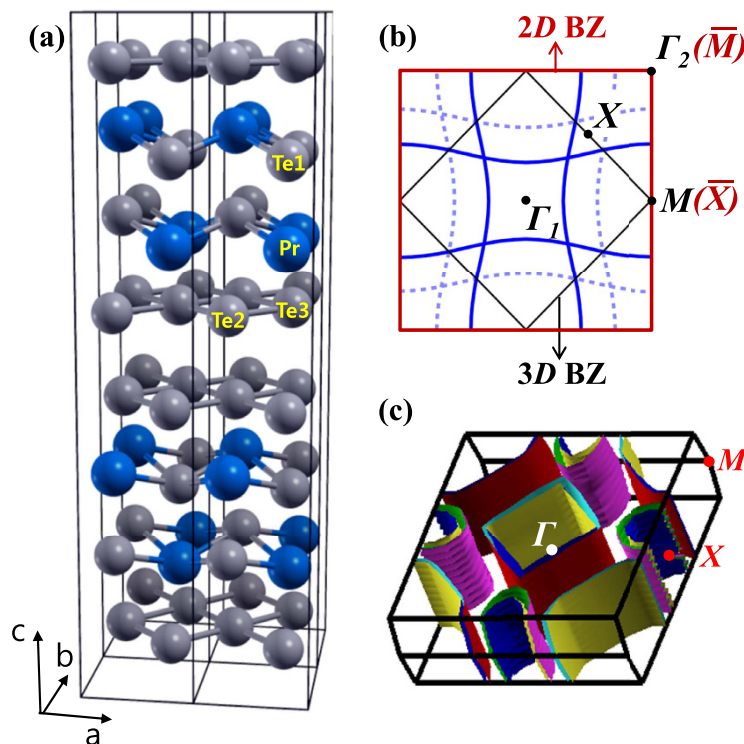


Figure 1. Crystal structure and the 2D/3D-Brillouin zones (BZs) of PrTe_3 . (a) Orthorhombic structure of PrTe_3 . (b) 2D Fermi surface for the undistorted (non-CDW) phase of PrTe_3 (denoted as the blue-solid lines). In orthorhombic PrTe_3 of (a), the unit cell of Te(2)-Te(3) square net is doubled. So the BZ of Te(2)-Te(3) sheets (the outer larger square, which we call as the 2D-BZ) is reduced to half and rotated by 45° (the inner smaller square, which we call as the 3D-BZ). The FS in the 2D-BZ is folded into the reduced 3D-BZ, to produce the folded-shadow FS, denoted as dotted lines. (c) 3D Fermi surface in the 3D-BZ of the undistorted PrTe_3 .

which are sandwiched along the c axis by the corrugated double layers of R and Te(1) atoms²⁴. Note that the convention of a , b , c in this work is different from that used in the literature for $R\text{Te}_3$. We have used this different convention to compare the crystal structure of PrTe_3 with that of $R\text{Te}_2$. Due to the presence of the R -Te(1) layer, the 2D unit cell of a Te(2)-Te(3) sheet is doubled ($\sqrt{2} \times \sqrt{2}$), resulting in a smaller Brillouin zone (BZ) (hereafter called as “3D-BZ”), reduced by half and rotated by 45° from the original 2D-BZ of the Te(2)-Te(3) square lattice. Then the shadow bands, which arise from the folding of the bands in the 2D-BZ into the 3D-BZ, are expected to appear in the reduced 3D-BZ. This feature is shown in Fig. 1(b), in which the FS in the outer 2D-BZ is folded into the inner 3D-BZ, to produce the 3D-folded shadow FS (denoted as dotted lines). Consequently, there appear two FSs, one inner (smaller) FS and the other outer (larger) FS. Around Γ_1 (in the first BZ of the reduced 3D-BZ), the intensity of the former is stronger than that of the latter, while vice versa around Γ_2 (in the second BZ of the 3D-BZ). In reality, if the interlayer interaction between Te(2)-Te(3) and R -Te(1) layers, which causes the band folding, is weak, the electronic structures of Te(2)-Te(3) sheets would keep the 2D nature of the planar square lattice, but would exhibit the 3D-like nature if the interlayer interactions become strong. A stronger interlayer interaction would yield a larger k_z dispersion²⁵.

The ionic configuration of $R\text{Te}_3$ is considered to be $R^{3+}\text{Te}(1)^{2-}\text{Te}(2)^{0.5-}\text{Te}(3)^{0.5-}$, but this conjecture has not been confirmed experimentally yet. If R ions are trivalent ($3+$), hole carriers are produced in the Te(2)-Te(3) sheets²⁶. Then, due to the partial filling, the square nets of two Te(2)-Te(3) planes are easily distorted by the Peierls-like mechanism²⁷. Band-structure calculations for a similar CDW system of $R\text{Te}_2$, which has only one partially-filled Te sheet, indicate that the CDW instability occurs from the FS nesting of the Te square sheets in the ab plane^{24,28-31}.

Despite extensive ARPES and related studies for $R\text{Te}_3$ ¹⁵⁻²³, some crucial issues remain to be resolved, listed as following. (i) The modulated structures of $R\text{Te}_3$ in the CDW phase has not been identified. (ii) The valence states of R ions in $R\text{Te}_3$ need be determined experimentally. (iii) The effects of the band foldings on the FS of Te(2)-Te(3) sheets, arising both from the interlayer interaction between Te(2)-Te(3) and R -Te(1) layers and from the CDW supercell formation, have not been sorted out yet. We have addressed these questions by performing careful measurements of ARPES, Pr $4d \rightarrow 4f$ resonant photoemission spectroscopy (RPES), and soft X-ray absorption spectroscopy (XAS) for high-quality stoichiometric single crystal of PrTe_3 , and first-principles electronic structure calculations and tight-binding (TB) model calculations for the CDW supercell structure. We have compared the data of PrTe_3 with those of PrTe_2 . Note that neither ARPES nor the band structure of PrTe_3 has been reported yet. Owing to the high-quality ARPES data, we were able to perform the state-of-art theoretical analysis so as to identify the modulated structure of PrTe_3 in the CDW phase.

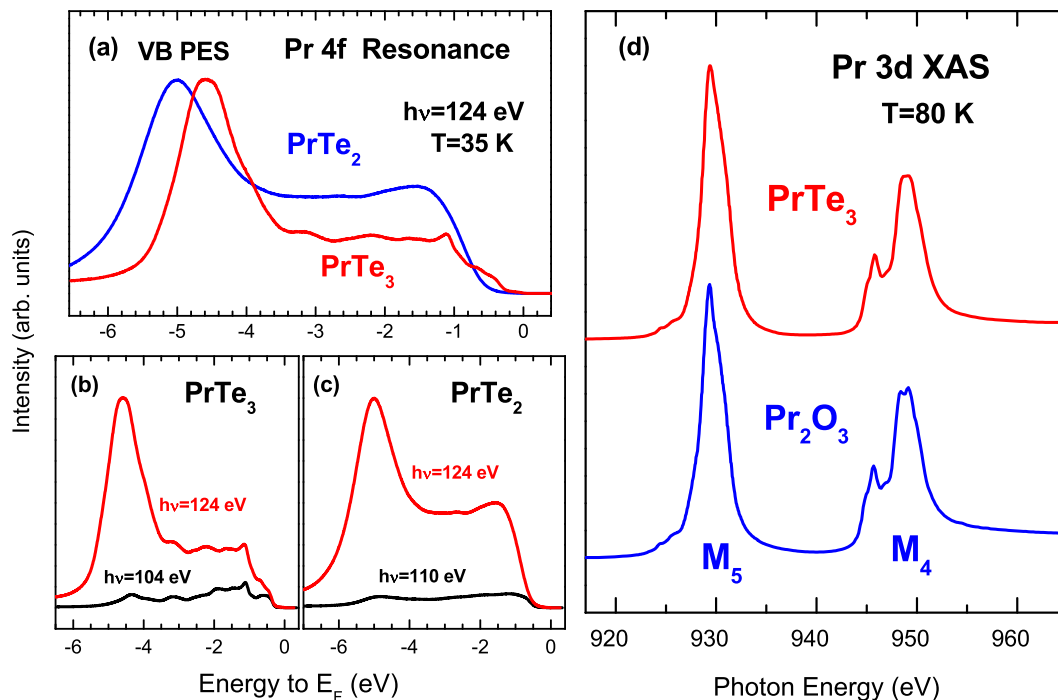


Figure 2. Pr 4fRPES and Pr 3d XAS spectra of PrTe₃. (a) Angle-integrated valence-band Pr 4d → 4f resonant photoemission spectroscopy (RPES) spectrum of PrTe₃, in comparison with that of PrTe₂. Both data were obtained at the Pr 4f resonance energy ($h\nu = 124$ eV). (b) Comparison of the Pr 4d → 4fRPES spectra of PrTe₃, obtained with $h\nu = 124$ eV (on-resonance) and $h\nu = 104$ eV (off the resonance), respectively. (c) Similarly for PrTe₂, obtained with $h\nu = 124$ eV (on-resonance) and $h\nu = 110$ eV (off the resonance), respectively. The PES spectra were obtained at $T = 35$ K and were normalized to the incident photon flux. (d) Comparison of the Pr 3d XAS spectrum of PrTe₃ with that of Pr₂O₃, obtained at $T = 80$ K.

Results

Figure 2(a) shows the angle-integrated valence-band PES spectrum of PrTe₃, compared to that of PrTe₂, obtained at the Pr 4f resonance energy ($h\nu = 124$ eV) in Pr 4d → 4fRPES. Here we include PrTe₂ as a reference system that has only one Te sheet in contrast to PrTe₃ that has two Te sheets. Fig. 2(b,c) compare the Pr 4d → 4f on-resonance spectra ($h\nu = 124$ eV) and those well below resonance (called “off-resonance”). The off-resonance spectra are dominated by the Te 5p emissions³². The Pr 4f PES spectra exhibit two prominent structures, one well below E_F (~ -5 eV) and the other at a low binding energy (BE) (~ -1 eV). The former Pr 4f peak well below E_F corresponds to the trivalent Pr $4f^{n_c m} \rightarrow 4f^{n-1} c^m$ transition (c : conduction-band electron, $n = 2$, $m = 3$), and is called as the “bare” Pr 4f peak. The latter Pr 4f structure at a lower BE (~ -1 eV) arises from the hybridization between Pr 4f and conduction-band electrons, corresponding to the $4f^{n_c m-1}$ final states^{33–35}, and is called as the hybridization peak. This identification for the latter Pr 4f structure is supported by the fact that the features of the low-BE Pr 4f structure resemble those of the off-resonance spectra³². Two major differences are observed between PrTe₃ and PrTe₂. First, the bare Pr 4f peak in PrTe₃ is located at a lower BE (~ -4.5 eV) than that in PrTe₂ (~ -5 eV). Secondly, PrTe₃ exhibits the finite Pr 4f spectral intensity near E_F , while PrTe₂ exhibits the negligible intensity near E_F . This trend is consistent with the resistivity data, where PrTe₃ is more metallic than PrTe₂. Our finding of the finite Pr 4f spectral intensity near E_F does not contradict the assumed picture of existing reports^{20,23}, where the R-Te(1) layers are considered to serve just as a charge reservoir. But the differences in the Pr 4f spectra between PrTe₃ and PrTe₂ indicate that the contribution from Pr 4f electrons to the CDW formation is larger in PrTe₃ than in PrTe₂. On the other hand, only the Te 5p states cross E_F , but the Pr 4f states do not, and so the Pr 4f contribution would be indirect, *i. e.*, Pr 4f electrons will contribute through the Pr 4f-Te(2)/Te(3) 5p hybridization. Hence PrTe₃ would have the stronger 3D nature than PrTe₂. It is also notable that the bare trivalent R^{3+} 4f states lie in deeper BE as R becomes heavier³⁶, resulting in the weaker R 4f-Te(2)/Te(3) 5p hybridization in R Te₃ having heavy R elements than in PrTe₃.

Figure 2(d) shows the Pr 3d (M -edge) XAS spectrum of PrTe₃, compared to that of trivalent reference oxide of Pr₂O₃. The Pr 3d XAS spectrum of PrTe₃ is found to be very similar to that of trivalent ($3+$) Pr₂O₃, indicating that Pr ions are nearly trivalent, having the $|g\rangle \approx |3d^{10}4f^2\rangle$ configuration in the ground state. Hence, Fig. 2(d) provides evidence that the valence states of Pr ions are nearly trivalent (Pr^{3+}) in PrTe₃, so that three electrons are donated per Pr ion. This finding supports the previous consensus that the R-Te(1) layers serve as charge reservoirs^{20,23}, as mentioned above. Two of the donated electrons will fill the Te 5p bands of the Pr-Te(1) layers, while one of them fills those of the Te(2)-Te(3) layers. This will result in the $R^{3+}Te(1)^{2-}Te(2)^{0.5-}Te(3)^{0.5-}$ configuration. The fully occupied Pr-Te(1) layers become semiconducting. In contrast, the partially filled Te(2)-Te(3) sheets become

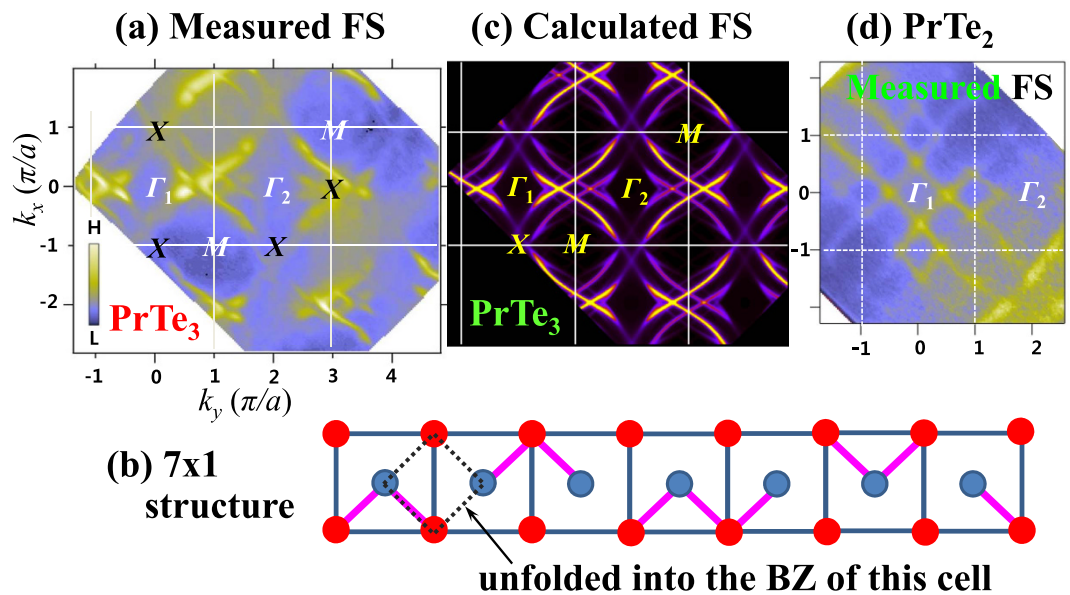


Figure 3. Comparison of the measured FS and the calculated FS for the CDW-distorted PrTe_3 . (a) The measured FS map of PrTe_3 over the wide BZ region, obtained with $h\nu = 104$ eV and at $T = 35$ K, which shows the two-fold symmetric FSs very clearly. Around Γ_1 , a smaller-size FS (the inner diamond) is stronger, while, around Γ_2 , a larger-size FS (the outer diamond) is stronger. (b) The candidate CDW-supercell structure having the 7×1 unit cell in the Te(2)-Te(3) sheets. Dumbbells, connected by red bars, represent the dimerized Te(2)-Te(3) atoms in the ab plane. Trimers and tetramers are seen to be the basic building blocks. (c) The calculated FS that is obtained from the tight-binding (TB) model for the CDW-distorted 7×1 supercell structure shown in (b) and unfolded into the 2D-BZ. (d) The measured FS map of PrTe_2 is shown for comparison, which was obtained with $h\nu = 110$ eV (corresponding to the Γ -plane of PrTe_2) and at $T = 35$ K.

metallic, which are easily distorted by the Peierls-like mechanism, as investigated by Papoian and Hoffmann³⁷. Hence this finding supports the CDW instability in the Te(2)-Te(3) sheets.

Figure 3 shows the measured FS map of PrTe_3 over the wide BZ region, in comparison with the calculated FS. The strong and weak FSs in Fig. 3(a), which are reversed in the first and second BZ, respectively, arise partly from the band folding due to the interaction of Te(2)-Te(3) bilayers with neighboring R-Te(1) layers. Such features are well established in literature^{16,19,30}. Then, the additional band folding on top of it arises from the CDW supercell structure. The measured FS in Fig. 3(a) appears to be anisotropic: the photoemission intensity around vertical X points ($\pm 1, 0$) is very weak (vanishes), while that around horizontal X points ($0, \pm 1$) is finite (strong). (Hereafter we call this feature as the “two-fold symmetric” FS feature.) The vanishing photoemission intensity in the FS is expected to arise from the CDW-induced FS reconstruction in the Te(2)-Te(3) sheet. Indeed the absence of the four-fold symmetry has been observed previously in several of RTe_3 ^{15,16,19,20}, which was then explained by the incommensurate CDW modulation vector^{15,16}. However, the CDW modulated structures that are responsible for such FSs have not been identified yet. So we have tried to determine the CDW modulated structures, as described in Fig. 3(b,c). As shown in Fig. S1 of Supplementary Information, a reasonably good agreement is found between the measured constant-energy (CE) maps (Fig. S1(a)) and the calculated CE maps for the non-CDW phase of an ideal Te square net (Fig. S1(b)). In contrast, a disagreement is found between the measured and calculated FSs. Such a disagreement comes from the fact that the calculated FS is obtained for the non-CDW phase of PrTe_3 , the structure of which is almost tetragonal (orthorhombic strictly). The two-fold symmetric FS of PrTe_3 makes a contrast with the four-fold symmetric FS of PrTe_2 , shown in Fig. 3(d).

For the CDW-distorted structure of PrTe_3 , the 7×1 structure has been once suggested to be a candidate in view of the observed 7-fold supercell structure in electron diffraction experiments for RTe_3 ^{38,39}. We would like to note, however that it is still under debate whether the CDW is uniformly incommensurate or locally commensurate within domains (*i.e.*, discommensurate)⁴⁰. There are two competing schools of thoughts regarding the lattice modulation in the CDW state. One school^{38,39} suggested the oligomer-type distortion of the Te(2)-Te(3) atoms in the CDW state, and argued that the CDW is discommensurate. The other school^{13,14} reported the long-range order arising from a smooth sinusoidal modulation of the Te-Te bonds (Te-Te dimers) and suggested a single incommensurate q_{CDW} . They argued that the CDW is uniformly incommensurate, which fits well with the FS nesting and Peierls-like distortion, but they did not provide the information on the distortion patterns of Te(2)-Te(3) atoms. Both schools present the similar q_{CDW} but for physically different reasons, *i.e.*, $q_{\text{CDW}} \sim 2/7a^*$. Hence, as a candidate CDW structure, we have considered the 7×1 supercell structure, which is large enough to take into account the local distortions of Te(2)-Te(3) atoms for the given $q_{\text{CDW}} \sim 2/7 a^*$.

Figure 3(c) shows the calculated FS of PrTe_3 , obtained from the TB model calculation for the assumed CDW-distorted 7×1 supercell structure shown in Fig. 3(b). In order to describe the 7×1 super-structure of PrTe_3 , we have first constructed a simple model TB Hamiltonian with the TB hopping parameters for the effective

p_x, p_y orbitals of Te atoms in the Te bilayer (Te sheets). To get the FS in Fig. 3(c), we have obtained the unfolded band structure by constructing the 7×1 Hamiltonian, diagonalizing it, and converting the Bloch factors into those of the cubic cell for the effective p_x/p_y orbitals, which are localized in each atomic position. As shown in Fig. 3(c), new features are observed near the $(0, \pm 1)$ points in the FS for the 7×1 structure, while gaps open at $(\pm 1, 0)$, resulting in the mirror symmetry, in contrast to the non-CDW FS of PrTe₃ (see Fig. S1(b) for the calculated non-CDW FS map.) Remarkably good agreement is found between the calculated FS for the assumed 7×1 supercell and the measured FS, indicating that the two-fold symmetric FS in PrTe₃ arises from the 7×1 modulated structure formation in the CDW phase.

Encouraged by the success in describing the experimental FS by combining the TB model and the unfolding technique⁴¹, we have performed the first-principles DFT calculation for a candidate CDW supercell of $7 \times 1 \times 1$ and then unfolded the calculated band structures. In the DFT calculations, Pr 4*f* electrons are treated as core electrons. Since the detailed structural data are not available in the literature, we have assumed both ferro-distortion and antiferro-distortion between the two layers in the bilayer, and then relaxed the $7 \times 1 \times 1$ supercell structure by using the VASP code. As for the relaxation calculation, we first assumed local distortions as presented in Fig. 3(b) and then let the system relax around this assumed structure. Interestingly, the shapes of Te-Te bondings (trimers and tetramers), as shown in Fig. 3(b), are maintained with the short and long Te-Te bond lengths being 3.071 Å and 3.084 Å, respectively, which are comparable to that (3.077 Å) in the non-CDW phase. This result indicates that the $7 \times 1 \times 1$ structure assumed in Fig. 3(b) is at least a metastable structure. It is also intriguing to note that the relaxed atomic positions maintaining oligomer patterns are described qualitatively well by the sinusoidal function with $q = 2/7a^*$ (see Fig. S2 of Supplementary Information), suggesting that the CDW structure of PrTe₃ can be described by either oligomers or sinusoidal distortions. Therefore, we think that the assumed $7 \times 1 \times 1$ supercell structure is close to the correct CDW structure of PrTe₃, as shown later in the comparison between the DFT-calculated band structures and ARPES. The energy difference between the ferro- and antiferro-cases is found to be negligibly small. Hence we have taken the antiferro-distorted structure for the DFT calculation.

The unfolded band structures calculated for the $1 \times 1 \times 1$ unit cell and the $7 \times 1 \times 1$ CDW-modulated supercell are shown in Fig. 4(a,b), respectively. Red guide lines in Fig. 4(a) represent the TB band structures for the Te square net. The red-, blue-, and green-colored arrows indicate the main band, the 3D-folded shadow band, and the CDW-folded shadow bands, respectively. The black-colored arrow in Fig. 4(b) indicates the calculated CDW gap. These results confirm the reproduction of the intensity differences between the first and second BZs, as observed in the measured ARPES.

The opening of the \vec{k} -dependent CDW gaps revealed in the FS are expected to appear in the energy distribution curves (EDCs) as the vanishing spectral intensity near E_F at certain \vec{k} points in the momentum space. Figure 5(a) shows the stack of EDCs of PrTe₃ for the near- E_F region along the diamond-shaped inner FS (along red dots, shown in the inset of Fig. 5(b)). In the EDC stacks, each EDC curve is shifted vertically. Some EDCs, selected from Fig. 5(a), are shown in Fig. 5(b). Guidelines (red lines) are superposed on these selected EDCs to show the \vec{k} -dependent movement of the peak positions and the accompanying intensity modulation near E_F ($I(E_F)$) better. The pronounced movement of the peak positions and the modulation of $I(E_F)$ at different \vec{k} points reflect the opening of the anisotropic energy gap, *i.e.* the \vec{k} -dependent gap $\Delta_g(\vec{k})$ in PrTe₃. These features are consistent with the findings of the measured FS (Fig. 3(a)).

Figure 6(a) compares the DFT-calculated band structures of PrTe₃ having the $7 \times 1 \times 1$ CDW-modulated supercell with the measured ARPES band structures, which are attached as the mirror images. The calculated band structures are unfolded into the 2D-BZ (see Fig. 1(b)) by utilizing the band-unfolding scheme⁴¹, so that the shadow bands are separated out from the main bands. Here Γ_1 and Γ_2 represent the Γ points in the first BZ and the second BZ (in the 3D-BZ notation), respectively. The left-side ARPES is that for the first BZ and the right-side ARPES is that for the second BZ. These ARPES image plots are the average of those obtained with the linear horizontal (LH) and linear vertical (LV) polarizations (see Fig. 7 below). As described above in Fig. 4, the dark and light colors in the calculated band structures denote the main bands and the shadow bands (both the 3D-folded shadow bands and the CDW-folded shadow bands), respectively. Figure 6(a) reveals that, with ~ -0.3 eV shift of the calculated E_F , the measured ARPES and the calculated band structures agree remarkably well in the dispersive band features and the energy positions. Further, the effect of the band folding, observed in ARPES, also agrees very well with that in the calculations. Thus these findings clearly indicate that the modulated structure of PrTe₃ in the CDW phase would be close to a $7 \times 1 \times 1$ supercell structure.

Figure 6(b) shows the ARPES image plots near E_F for both the first BZ (left) and the second BZ (right) separately. Both data were obtained with the LH polarization. Figure 6(b) reveals the following features. First, the bands crossing through E_F are observed clearly, which are responsible for determining the FS at the corresponding \vec{k}_F values. The E_F -crossing positions in ARPES agree with those in the calculated bands for the non-CDW phase of PrTe₃ (see Fig. 6(a)) very well, which have mainly the Te(2)-Te(3) in-plane 5*p* character. Two crossing bands are observed along ΓM , one near $\sim 0.2 \Gamma M$ (marked with a red arrow in (b)) and the other at $\sim 0.55 \Gamma M$ (marked with a blue arrow in (b)). They produce the inner FS and outer FS, respectively, as shown in Fig. 1(b). Note that the spectral intensities of these two crossing bands in the first BZ (left) become reversed in the second BZ (right). Hence Fig. 6 provides evidence for the band folding due to the interlayer interaction of Te(2)-Te(3) layers with Pr-Te(1) layers in PrTe₃.

In contrast to the previous ARPES work on $R\text{Te}_3$ ($R = \text{Ce}, \text{Tb}, \text{Y}$)²⁰, the bilayer splitting is not clearly observed in our near- E_F ARPES image plots in the Γ plane within the experimental resolution. Considering the energy and k -resolution employed in this work ($\Delta E \lesssim 40$ meV and $\Delta k \lesssim 0.012 \text{ \AA}^{-1}$ (*i.e.*, $\Delta k \lesssim 0.009 \frac{2\pi}{a}$ along ΓM)), this observation suggests that the size of the bilayer splitting near E_F is less than the above experimental resolutions in

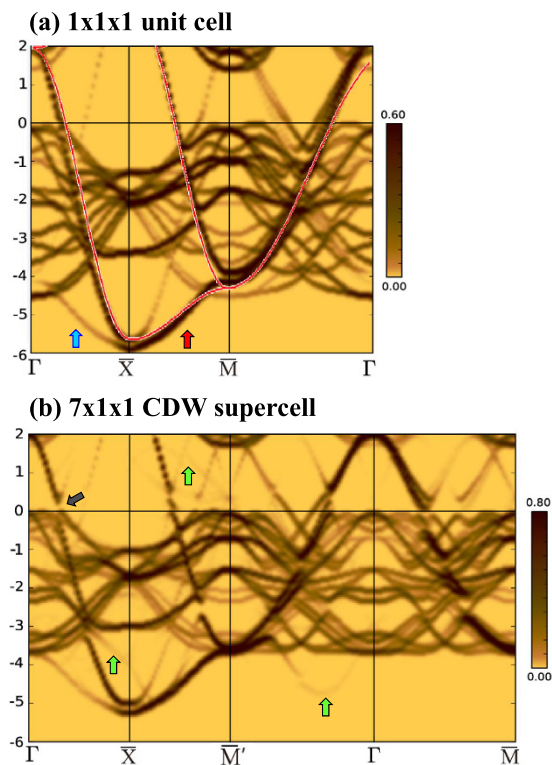


Figure 4. Calculated band structures of PrTe_3 unfolded into the 2D-BZ. (a) Band structure of PrTe_3 calculated for the $1 \times 1 \times 1$ unit cell, and (b) Band structure of PrTe_3 calculated for the $7 \times 1 \times 1$ CDW-modulated supercell. \bar{M} is along a^* (see Fig. 1(b)), while \bar{M}' is along b^* that is perpendicular to the CDW vector q_{CDW} . Red guide lines in (a) represent the TB band structure for the Te square net. The colored arrows indicate the main band (red), the 3D-folded shadow band (blue), the CDW-folded shadow band (green), and the CDW gap (black), respectively. To show the CDW gap more clearly, we considered the 20%-expanded volume of the $7 \times 1 \times 1$ cell in (b).

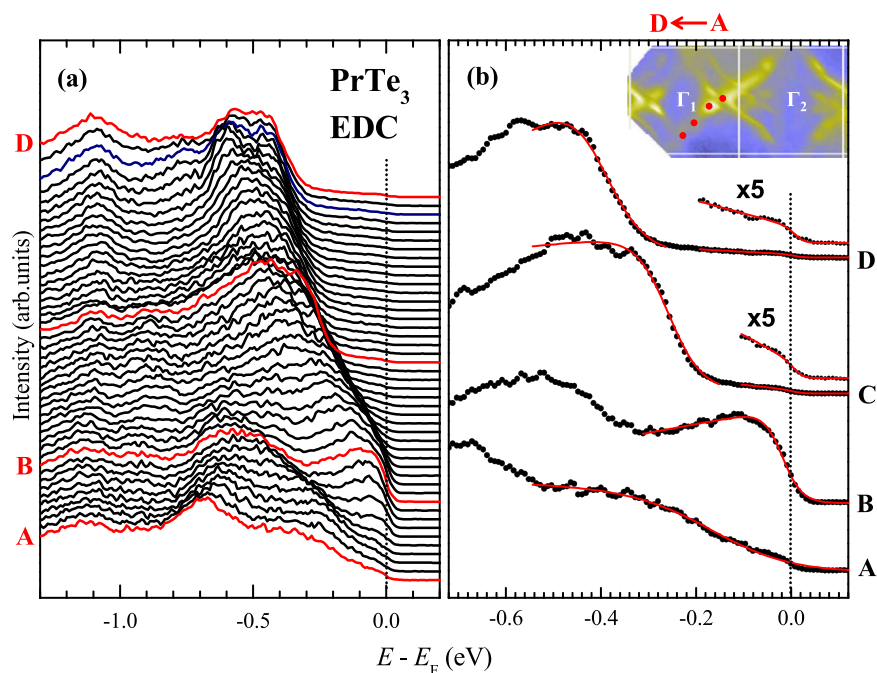


Figure 5. Near- E_F EDCs for PrTe_3 . (a) The near- E_F EDC stacks for PrTe_3 , obtained with $h\nu = 104$ eV and at $T = 35$ K, along the inner diamond-shaped FS ($A \rightarrow D$), which is shown in the inset of (b) as the red dots. (b) Some EDCs selected from (a), on which guidelines (red lines) are superposed. For the EDCs obtained at C and D, the near- E_F regions are enlarged by $\times 5$.

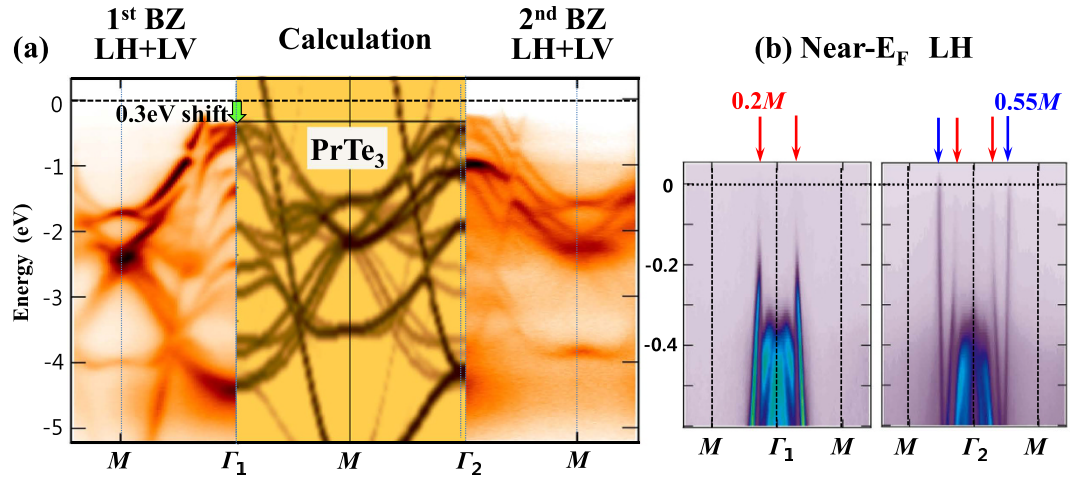


Figure 6. Comparison of the DFT-calculated band structures for the $7 \times 1 \times 1$ CDW-modulated supercell of PrTe_3 with ARPES ($T = 35$ K). The calculated bands are unfolded into the 2D-BZ. (a) The calculated band structures for the $7 \times 1 \times 1$ CDW-modulated supercell of PrTe_3 along $\Gamma_1 M \Gamma_2$ (in the 3D-BZ notation of Fig. 1(b)), which are attached to the measured ARPES as mirror images. The ARPES image plots on the left and right sides are those for the first BZ and the second BZ, respectively. In the calculated band structures, the dark and light colors denote the main bands and the shadow bands (both the 3D-folded shadow bands and the CDW-folded shadow bands), respectively. ARPES data were obtained with $h\nu = 104$ eV and at $T = 35$ K. Nearly perfect agreement is obtained with the ~ 0.3 eV shift of the calculated E_F . (b) The measured ARPES image plots for the energy region near E_F for the first BZ (left) and for the second BZ (right). Two crossing bands are observed along ΓM , one near $\sim 0.2 \Gamma M$ (marked with red arrows) and the other at $\sim 0.55 \Gamma M$ (marked with blue arrows).

PrTe_3 . In the previous ARPES work on $R\text{Te}_3$ ($R = \text{Ce}, \text{Tb}, \text{Y}$)²⁰, quite a large bilayer splitting was reported along ΓX ($\Delta k \sim 0.025 \frac{2\pi}{a}$ and $\Delta E \geq 0.1$ eV). Our calculations for PrTe_3 , with the spin-orbit coupling (SOC) included, reveal that the size of the bilayer splitting near E_F is ~ 0.1 eV. But, due to the very dispersive band nature, the splitting of these bands corresponds to $\Delta k \lesssim 0.01 \text{ \AA}^{-1}$ and so it is hardly seen even in the calculated band structures. The difficulty in resolving the bilayer splitting in ARPES is expected to be related to such a very dispersive band nature.

Figure 7 shows the effects of linear dichroism (LD) and circular dichroism (CD) in the measured ARPES of PrTe_3 . Figure 7(a–c) show the measured ARPES image plots of PrTe_3 along $M\Gamma M$ (in the 1st BZ), obtained with two different polarizations of LH and LV polarizations, and the difference between them, respectively. The schematic drawings on the left show the configurations for LH and LV polarizations. In the LH configuration, the electric field vector \vec{E} of the incident photons has a perpendicular component to the sample surface, while \vec{E} is always parallel to the sample surface in the LV configuration. The difference between LH and LV is defined as linear dichroism (LD) $\text{LD} \equiv \text{LH} - \text{LV}$. Similarly, Fig. 7(d–f) show the measured ARPES image plots of PrTe_3 , obtained with right circular (RC) and left circular (LC) polarizations, and the difference between them, respectively. The difference between RC and LC is defined as circular dichroism (CD) $\text{CD} \equiv \text{RC} - \text{LC}$.

The dichroic ARPES image plots for PrTe_3 reveal several features. (i) Very dispersive bands are observed in ARPES of PrTe_3 and the large-energy-scale band structures of PrTe_3 are very similar to those of $R\text{Te}_2$ ($R = \text{Ce}, \text{Pr}$)^{30,42}. (ii) The effects of both the LD and CD are observed clearly. The states at $-1 \text{ eV} \lesssim E_i \lesssim -0.2 \text{ eV}$ near Γ exhibit the stronger intensity with the LH polarization than with the LV polarization, while the nearly straight bands near M from ~ -4 eV below exhibit the opposite trend. The observed LD in ARPES implies that the orbitals around -0.5 eV and -4 eV below are ordered mainly along the c axis and in the ab plane, respectively. A closer look at the ARPES near E_F shows that, similarly as in PrTe_2 ⁴², the E_F -crossing bands exhibit the stronger intensity with the LV polarization than with the LH polarization. As described above, \vec{E} of the incident photons is nearly perpendicular to and parallel to the sample surface with the LH and LV polarizations, respectively (see Fig. 7 Left). Therefore the observation of the stronger intensity with the LV polarization implies that the E_F -crossing orbitals are ordered mainly parallel to the sample surface, *i. e.*, in the ab plane rather than along the c axis.

The effect of CD ($\text{CD} \equiv \text{RC} - \text{LC}$) is more complicated than that of LD. The E_F -crossing states along (110) have a stronger RC character while those along $(\bar{1}\bar{1}0)$ have a stronger LC character. The states at ~ -2 eV show the opposite CD effect. It has been reported that the CD effect arises from the experimental geometry, namely, the experimental handedness⁴³. On the other hand, there was also a proposal that the CD arises from the local orbital angular momentum of a system⁴⁴. Hence, there is no general theory yet, which explains the CD effects observed in various systems. If the observed CD has the intrinsic origin partly, the local orbital angular momentum of the Te $5p$ states would be finite in the CDW states of PrTe_3 . However, the nonmagnetic CDW states of $R\text{Te}_3$ seem to refute this idea. Therefore, further theoretical analysis is required to elucidate the origin and the physical meaning of the CD effect in PrTe_3 .

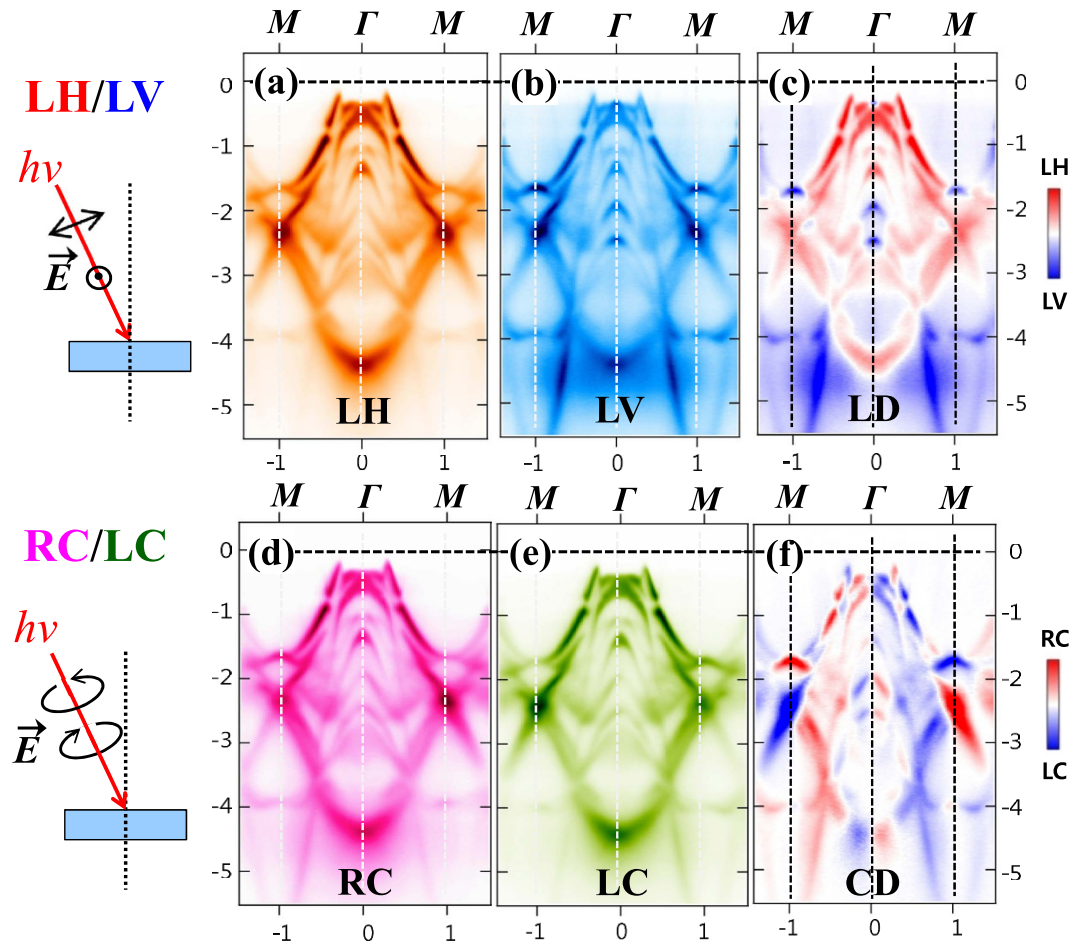


Figure 7. Linear Dichroism (LD) and Circular Dichroism (CD) in ARPES. (a–c) The measured ARPES image plots of PrTe₃ along $M\Gamma M$ (in the first BZ), obtained with the LH and LV polarization, and the difference (LD) between the LH and LV ARPES ($LD \equiv LH - LV$), respectively. (d–f) Similarly for the right circular (RC) and left circular (LC) polarization, and their differences (CD), respectively ($CD \equiv RC - LC$). These data were obtained with $h\nu = 104$ eV and at $T = 35$ K. The schematic drawings on the left show the configurations for LH/LV and RC/LC measurements. In the LD and CD ARPES plots ((c,f)), red color represents the stronger LH/RC intensity and blue color represents the stronger LV/LC intensity.

Figure 8(a,b) show the $k_x - k_z$ plane in the BZ of PrTe₃, for which the $h\nu$ -map was obtained, and the calculated FS for PrTe₃, respectively. Figure 8(c) shows the measured Fermi-edge $h\nu(k_z)$ map²⁵ between 80–120 eV with the horizontal direction parallel to (100). Hence Fig. 8(c) represents the measured FS for the BZ of $XTX-RZR$, as shown in Fig. 8(a). The measured $k_x - k_z$ ($h\nu$) map for the E_F -crossing states in PrTe₃, exhibits the straight vertical dispersions along k_z , indicating that they have the nearly 2D-like character, and that the interaction between Pr-Te(1) layer and Te(2)-Te(3) layers does not have a crucial contribution to the electronic states responsible for the CDW formation in PrTe₃. The calculated FS of PrTe₃ in Fig. 8(b) also shows the straight vertical dispersions along k_z . However, an extra lens-like FS, which is present in the calculated FS (Fig. 8(b)), is not observed in the measured FS (Fig. 8(c)). The existence of this lens-like FS need be checked more carefully.

Finally, it is worthwhile to address an important issue in $R\text{Te}_3$, namely, why there exist two-step vs single-step CDW transitions depending on the R elements. As mentioned above, $R\text{Te}_3$ has a nearly tetragonal structure, and so there exist two competing FS nesting vectors, q_{1-CDW} and q_{2-CDW} , along a^* and b^* directions, respectively. But, due to the lattice strain energy, one direction is thought to be selected first for the CDW transition⁴⁵. However, for heavy $R\text{Te}_3$ having smaller volumes, the FS nesting is far more imperfect than for light $R\text{Te}_3$ having larger volumes, and so there still remains the possibility of the second CDW transition to occur even after the first CDW transition. This would be the reason why there exist two-step transitions for $R = \text{Dy-Tm}$ while only single-step transitions for $R = \text{Ce-Tb}$. These features, together with the reduced densities of states at E_F for heavy $R\text{Te}_3$, are also consistent with the reduced first T_{CDW} for heavy $R\text{Te}_3$. This idea deserves to be checked more systematically further in future.

Conclusion

The electronic structure of PrTe₃ has been investigated by employing ARPES, XAS, RPES, and first-principles band structure calculation, and the questions addressed in Introduction are answered. In particular, a possible

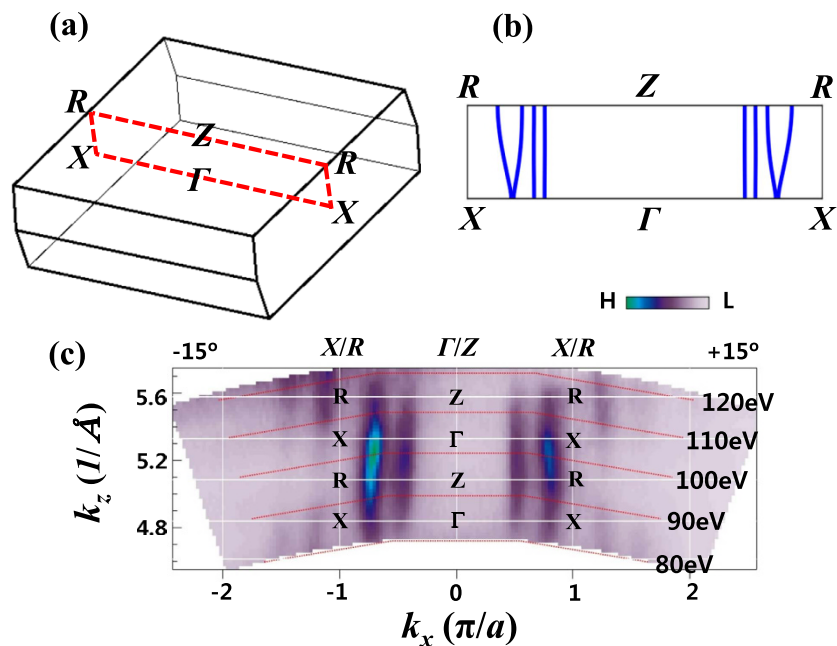


Figure 8. Photon Energy Map. (a) The $k_x - k_z$ plane for which the $h\nu$ -map was obtained in the BZ of PrTe_3 . The colored plane represents where the $h\nu$ -map was obtained. (b) The calculated FS for the $k_x - k_z$ BZ in PrTe_3 . The 2D cylindrical FSs come from the in-plane p bands of Te(2) and Te(3) in the Te square net, while the outmost dispersive FS comes from the mixture of the out-of-plane p bands of Te(1) and the in-plane p bands of Te(2) and Te(3). (c) The Fermi-edge state $h\nu$ -map for PrTe_3 , obtained for $h\nu$ between 80–120 eV and at $T = 35$ K. The horizontal k_x direction is parallel to (100). This $h\nu$ -map cuts through $X\Gamma X$ (RZR) along k_z ($h\nu$).

candidate of the modulated structure of PrTe_3 in the CDW phase has been identified Pr $3d$ XAS measurement provides evidence that the valence states of Pr ions are nearly trivalent (Pr^{3+}) in PrTe_3 , supporting the previous consensus of the R-Te(1) layer being a charge reservoir, and the CDW instability in the partially-filled metallic Te(2)-Te(3) sheets. Pr $4d \rightarrow 4f$ RPES measurement reveals the finite Pr $4f$ spectral intensity near E_F , making a contrast to the negligible near- E_F intensity in PrTe_2 , which has one Te sheet only. This finding indicates the larger Pr $4f$ contribution to the CDW formation in PrTe_3 than that in PrTe_2 through the Pr $4f$ -Te(2)/Te(3) $5p$ hybridization. The two-fold symmetric FS has been clearly observed in PrTe_3 , which arises from the CDW-induced FS reconstruction. The CDW modulated structure in PrTe_3 is likely to be the 7×1 structure (see Fig. 3(b)). The shadow bands and the corresponding very weak FSs are observed, originating from the band folding due to the interaction of Te(2)-Te(3) layers with Pr-Te(1) layers and also that due to the CDW-induced FS reconstruction. The effects of both LD and CD are observed in ARPES. The opposite effects of LD are observed between the E_F -crossing states and the states at ~ 1 eV BE. The E_F -crossing bands exhibit the stronger intensity with the LV polarization than with the LH polarization, implying that the E_F -crossing orbitals are ordered mainly in the ab plane, but not along the c axis. The observed CD in ARPES seems to reflect the existence of the experimental geometry effect, which, however, remains to be resolved theoretically. The straight vertical dispersions are observed along k_z in the $k_x - k_z$ ($h\nu$) FS map, which demonstrates the 2D character for the near- E_F states in PrTe_3 . This finding implies the weak 3D interaction between Pr-Te(1) layer and Te(2)-Te(3) layers in PrTe_3 .

Methods

Sample Growth. High-quality PrTe_3 single crystals were grown by using the self-fluxed Bridgeman method⁴⁶. The quality and the orientation of the single crystal were checked by Laue patterns. PrTe_3 has nearly the same lattice constants for the ab plane, but much larger lattice constant along the c axis due to the magnetic ordering along c : $a = 4.375 \text{ \AA}$ and $c = 25.89 \text{ \AA}$ ^{14,47}.

ARPES and XAS Experiment. ARPES measurements were carried out at the MERLIN beamline 4.0.3 at the Advanced Light Source (ALS). The ARPES endstation is equipped with a Scienta R8000 electron energy analyzer and a low temperature 6-axis sample manipulator cooled with an open-cycle He flow cryostat. Samples can be cooled down to 6 K, but we kept the samples at $T \sim 35$ K to improve the electrical conductivity of them. Single crystalline samples were cleaved *in situ* and measured under the pressure better than 5×10^{-11} Torr. The photon energy ($h\nu$) corresponding to the Γ plane was determined from the photon energy scans for the Fermi-edge states at the normal emission⁴⁸. For PrTe_3 , $h\nu \approx 104$ eV turned out to be close to the Γ plane within the experimental uncertainty (see Fig. 8). The Fermi level (E_F) and the instrumental resolution of the system were determined from the Fermi edge spectrum of an evaporated Au metal. The energy resolution of the data was set at ~ 40 meV for $h\nu = 104$ eV. The momentum resolution (k -resolution Δk) of the data was set to be less than $\Delta k \leq 0.012 \text{ \AA}^{-1}$ in the detector angle. The $k_x - k_y$ FS maps were obtained in the polar-compensation mode.

XAS experiment was performed at the 2A elliptically polarized undulator (EPU) beamline of the Pohang Light Source (PLS). XAS data were obtained by using the total electron yield (TEY) mode. Single crystalline samples were cleaved *in situ* and measured under the pressure better than 3×10^{-10} Torr and at $T \sim 80$ K. The total resolution for XAS was set at ~ 100 meV at $h\nu \sim 600$ eV. All the spectra were normalized to the incident photon flux.

DFT and Tight-Binding (TB) Model Calculations. For density functional theory (DFT) band calculations, we employed the *ab-initio* full-potential linearized augmented (FLAPW) band method implemented in Wien2k⁴⁹. The pseudopotential band method implemented in VASP⁵⁰ was also used for the band-unfolding⁴¹. The generalized-gradient approximation (GGA) was utilized for the exchange-correlation interaction, and the spin-orbit interaction was taken into account in the second variation manner.

For the TB model calculations, for simplicity, we have ignored the small corrugation of Te atoms in the Te bilayer, and considered the single Te layer only. The p_z orbitals are ignored because these orbitals are far from E_F . The effect of the lattice distortion is ignored in this simple TB model. The TB hopping parameters of (pp_σ ; pp_π) for the long and short bonds are taken as (1.4; -0.5) and (2.0; -0.3), respectively.

References

1. Voit, J. *et al.* Electronic Structure of Solids with Competing Periodic Potentials. *Science* **290**, 501 (2000).
2. Kasuya, T., Jung, M. H. & Takabatake, T. Charge density wave and excitonic magnetic polarons in CeTe₂. *J. Magn. Magn. Mater.* **220**, 235 (2000).
3. Ashcroft, N. W. & Mermin, N. D. *Solid State Physics* (Holt, Rinehart and Winston, 1976).
4. Yao, H., Robertson, J. A., Kim, E. A. & Kivelson, S. A. Theory of stripes in quasi-two dimensional rare-earth tellurides. *Phys. Rev. B* **74**, 245126 (2006).
5. Yokoya, T. *et al.* Fermi surface sheet-dependent superconductivity in 2H-NbSe₂. *Science* **294**, 2518 (2001).
6. Gabovich, A. M., Voitenko, A. I. & Ausloos, M. Charge- and spin-density waves in existing superconductors: competition between Cooper pairing and Peierls or excitonic instabilities. *Phys. Rep.* **367**, 583 (2002).
7. Aebi, P., Pillo, Th., Berger, H. & Levy, F. On the search for Fermi surface nesting in quasi-2D materials. *J. Electron Spectrosc. Relat. Phenom.* **117–118**, 433 (2001).
8. Johannes, M. D. & Mazin, I. I. Fermi surface nesting and the origin of charge density waves in metal. *Phys. Rev. B* **77**, 165135 (2008).
9. Rossnagel, K. On the origin of charge-density waves in select layered transition-metal dichalcogenides. *J. Phys.: Condens. Matter* **23**, 213001 (2011).
10. Hellmann, S. *et al.* Time-domain classification of charge-density-wave insulators. *Nature Commun.* **3**, 1069 (2012).
11. Perfetti, L., Gloor, T. A., Mila, F., Berger, H. & Grioni, M. Unexpected periodicity in the quasi-two-dimensional Mott insulator 1T-TaS₂ revealed by angle-resolved photoemission. *Phys. Rev. B* **71**, 153101 (2005).
12. Kim, H. J. *et al.* Local atomic structure and discommensurations in the charge density wave of CeTe₃. *Phys. Rev. Lett.* **96**, 226401 (2006).
13. Fang, A., Ru, N., Fisher, I. R. & Kapitulnik, A. STM studies of TbTe₃: evidence for a fully incommensurate charge density wave. *Phys. Rev. Lett.* **99**, 046401 (2007).
14. Ru, N. *et al.* Effect of chemical pressure on the charge density wave transition in rare-earth tritellurides RTe₃. *Phys. Rev. B* **77**, 035114 (2008).
15. Gweon, G.-H. *et al.* Direct observation of complete Fermi surface, imperfect nesting, and gap anisotropy in the high-temperature incommensurate charge-density-wave compound SmTe₃. *Phys. Rev. Lett.* **81**, 886 (1998).
16. Brouet, V. *et al.* Fermi surface reconstruction in the CDW states of CeTe₃ observed by photoemission. *Phys. Rev. Lett.* **93**, 126405 (2004).
17. Komoda, H. *et al.* High-resolution angle-resolved photoemission study of incommensurate charge-density-wave compound CeTe₃. *Phys. Rev. B* **70**, 195101 (2004).
18. Laverock, J. *et al.* Fermi surface nesting and charge-density wave formation in rare-earth tritellurides. *Phys. Rev. B* **71**, 085114 (2005).
19. Shin, K. Y., Brouet, V., Ru, N., Shen, Z. X. & Fisher, I. R. Electronic structure and charge-density wave formation in LaTe_{1.95} and CeTe_{2.00}. *Phys. Rev. B* **72**, 085132 (2005).
20. Brouet, V. *et al.* Angle-resolved photoemission study of the evolution of band structure and charge density wave properties in RTe₃ (R = Y, La, Ce, Sm, Gd, Tb, and Dy). *Phys. Rev. B* **77**, 235104 (2008). See references therein.
21. Schmitt, F. *et al.* Transient electronic structure and melting of a charge density wave in TbTe₃. *Science* **321**, 1649 (2008).
22. Moore, R. G. *et al.* Fermi surface evolution across multiple charge density wave transitions in ErTe₃. *Phys. Rev. B* **81**, 073102 (2010).
23. Eiter, H.-M. *et al.* Alternative route to charge density wave formation in multiband systems. *Proc. Natl. Acad. Sci.* **110**, 64 (2013).
24. Kikuchi, A. Electronic Structure of Lanthan Ditellurides. *J. Phys. Soc. Jpn.* **67**, 1308 (1998).
25. Ito, T., Im, Hojun, Kimura, S.-I. & Kwon, Y. S. Three-dimensional Fermi-surface of CeTe₂ studied by angle-resolved photoemission. *J. Magn. Magn. Mater.* **310**, 431 (2007).
26. Kang, J.-S., Olson, C. G., Kwon, Y. S., Shim, J. H. & Min, B. I. Charge-density wave gap and Ce 4f states in CeTe₂ observed by photoemission spectroscopy. *Phys. Rev. B* **74**, 085115 (2006).
27. Burdett J. K. & Lee, S. Peierls Distortions in Two and Three Dimensions and the Structures of AB Solids. *J. Amer. Chem. Soc.* **105**, 1079 (1983).
28. DiMasi, E., Foran, B., Aronson, M. C. & Lee, S. Stability of charge-density waves under continuous variation of band filling in LaTe_{2-x}Sb_x (0 ≤ x ≤ 1). *Phys. Rev. B* **54**, 13587 (1996).
29. Shim, J. H., Kang, J.-S. & Min, B. I. Electronic structures of RTe₂ (R = La, Ce): A Clue to the pressure-Induced superconductivity in CeTe_{1.82}. *Phys. Rev. Lett.* **93**, 156406 (2004).
30. Kang, J.-S. *et al.* Fermi surface reconstruction in CeTe₂ induced by charge density waves investigated via angle resolved photoemission. *Phys. Rev. B* **85**, 085104 (2012).
31. Stöwe, K. Crystal structure and magnetic properties of CeTe₂. *J. Alloy Compd.* **307**, 101 (2000); Crystal structure and electronic band structure of LaTe₂. *J. Solid State Chem.* **149**, 155 (2000).
32. J. J. Yeh & I. Lindau *At. Data Nucl. Data Tables* **32**, 1 (1985).
33. Gunnarsson, O. & Schönhammer, K. Electron spectroscopies for Ce compounds in the impurity model. *Phys. Rev. B* **28**, 4315 (1983).
34. Norman, M. R. *et al.* Origin of the two-peak photoemission and inverse-photoemission spectra in Ce and Ce compounds. *Phys. Rev. Lett.* **53**, 1673 (1984).
35. Allen, J. W. *et al.* Electronic structure of cerium and light rare-earth intermetallics. *Adv. Phys.* **35**, 275 (1987).
36. Lang, J. K., Baer, Y. & Cox, P. A. Study of the 4f and valence band density of states in rare-earth metals. II. Experiment and results. *J. Phys. F: Metal Phys.* **11**, 121 (1981).
37. Papoian, G. A. & Hoffmann, R. Hypervalent Bonding in One, Two, and Three Dimensions: Extending the Zintl-Klemm Concept to Nonclassical Electron-Rich Networks. *Angew. Chem. Int. Ed.* **39**, 2408 (2000).

38. Malliakas, C., Billinge, S. J. L., Kim, H. J. & Kanatzidis, M. G. Square nets of tellurium: rare-earth dependent variation in the charge-density wave of RETe₃ (RE=rare-earth element). *J. Amer. Chem. Soc.* **127**, 6510 (2005).
39. Malliakas, C. D. & Kanatzidis, M. G. Divergence in the Behavior of the Charge Density Wave in RETe₃ (RE=Rare-Earth Element) with Temperature and RE Element. *J. Amer. Chem. Soc.* **128**, 12612 (2006).
40. Tomic, A. *et al.* Scanning tunneling microscopy study of the CeTe₃ charge density wave. *Phys. Rev. B* **77**, 085422 (2009).
41. Ku, W., Berlijn, T. & Lee, C.-C. Unfolding first-principles band structures. *Phys. Rev. Lett.* **104**, 216401 (2010).
42. Lee, Eunsook *et al.* Angle-resolved and resonant photoemission spectroscopy study of the Fermi surface reconstruction in the charge density wave systems of CeTe₂ and PrTe₂. *Phys. Rev. B* **91**, 125137 (2015).
43. Schönhense, G. Circular dichroism and spin polarization in photoemission from adsorbates and non-magnetic solid. *Phys. Scr.* **T31**, 255 (1990).
44. Park, S. R., Kim, C. H., Yu, J., Han, J. H. & Kim, C. Orbital angular-momentum based origin of Rashba-type surface band splitting. *Phys. Rev. Lett.* **107**, 156803 (2011).
45. Moore, R. G. *et al.* Ultrafast resonant soft x-ray diffraction dynamics of the charge density wave in TbTe₃. *Phys. Rev. B* **93**, 024304 (2016).
46. Min, B. H., Choi, H. Y. & Kwon, Y. S. Anomalous magnetization in CeTe₂. *Physica B* **312–313**, 203 (2002).
47. Lavagnini, M. Ph. D. Thesis, "Optics at high pressures in Charge-Density-Wave systems", Swiss Federal Institute of Technology, Zurich (2009).
48. Denlinger, J. D. *et al.* SmB₆ photoemission: past and present. *J. Phys. Soc. Jpn. Conf. Proc.* **3**, 017038 (2014).
49. Blaha, P. *et al.* WIEN2k, An Augmented Plane Wave Plus Local Orbitals Program for Calculating Crystal Properties. ISBN 3-9501031-1-1, Karlheinz Schwarz, Techn. Universität Wien, Austria (2001).
50. Kresse, G. & Furthmüller, J. Efficient iterative schemes for ab initio total-energy calculations using a plane-wave basis set. *Phys. Rev. B* **54**, 11169 (1996).

Acknowledgements

This work was supported by the NRF under Contract No. 2014R1A1A2056546, No. 2015R1A2A1A15053564, and No. 2011-0025237, and also by the KISTI supercomputing center (No. KSC-2015-C3-068). The ALS is supported by U.S. DOE under Contract No. DE-AC02-05CH11231. BHM and YSK were supported by the Basic Science Research Program of the NRF (2013R1A1A2009778). The travel for the ARPES experiment at the ALS was supported in part by MSIP and PAL in Korea.

Author Contributions

E.L., D.H.K., H.W.K., J.D.D. and J.-S.K. performed ARPES, XAS and RPES experiment. B.H.M. and Y.S.K. prepared and characterized single crystalline samples. H.K., J.K., K.K. and B.I.M. did DFT and TB calculations. E.L., J.-S.K., K.K. and B.I.M. wrote the manuscript. All authors discussed the results and reviewed the manuscript.

Additional Information

Supplementary information accompanies this paper at <http://www.nature.com/srep>

Competing financial interests: The authors declare no competing financial interests.

How to cite this article: Lee, E. *et al.* The 7 × 1 Fermi Surface Reconstruction in a Two-dimensional *f*-electron Charge Density Wave System: PrTe₃. *Sci. Rep.* **6**, 30318; doi: 10.1038/srep30318 (2016).



This work is licensed under a Creative Commons Attribution 4.0 International License. The images or other third party material in this article are included in the article's Creative Commons license, unless indicated otherwise in the credit line; if the material is not included under the Creative Commons license, users will need to obtain permission from the license holder to reproduce the material. To view a copy of this license, visit <http://creativecommons.org/licenses/by/4.0/>

© The Author(s) 2016